T_1 Anisotropy Elucidates Spin Relaxation Mechanisms in an S = 1 Cr(IV) Optically Addressable Molecular Qubit

Nathanael P. Kazmierczak[†], Kaitlin M. Luedecke[†], Elisabeth T. Gallmeier, and Ryan G. Hadt*

Division of Chemistry and Chemical Engineering, Arthur Amos Noyes Laboratory of Chemical Physics, California Institute of Technology, Pasadena, California 91125, United States

[†]Co-first authors

*Corresponding author: rghadt@caltech.edu

Abstract: Paramagnetic molecules offer unique advantages for quantum information science owing to their spatial compactness, synthetic tunability, room-temperature quantum coherence, and potential for optical state initialization and readout. However, current optically addressable molecular qubits are hampered by rapid spin-lattice relaxation (T_1) even at sub-liquid nitrogen temperatures. Here we use temperature- and orientation-dependent pulsed electron paramagnetic resonance (EPR) to elucidate the negative sign of the ground-state zero-field splitting (ZFS) and assign T_1 anisotropy to specific degrees of freedom in an optically addressable S = 1 Cr(IV) molecular qubit. The anisotropy displays a distinct $\sin^2(2\theta)$ functional form that is not observed in S = ½ Cu(II) or V(IV) microwave addressable molecular qubits. The Cr(IV) T_1 anisotropy is ascribed to couplings between electron spins and rotational motion in low-energy acoustic or pseudo-acoustic phonons. Our findings suggest that rotational degrees of freedom should be suppressed to maximize the coherence temperature of optically addressable qubits.

The anionic nitrogen vacancy (NV^-) center in diamond constitutes one of the most widely implemented platforms for quantum sensing and imaging.[1] Substitutional replacement of two carbons in the diamond lattice with a nitrogen and a vacancy forms an S = 1 paramagnetic defect that exhibits selective photoluminescence behavior depending on the Zeeman sublevel that the spin occupies.[2,3] Furthermore, optical excitation of the NV^- center accumulates ground state spin polarization through a spin-selective intersystem crossing mechanism. These two features enable optical initialization and detection of quantum states in the Zeeman sublevels of the S = 1 defect, permitting a much greater degree of spatial localization than can be achieved with direct resonant microwave readout of the Zeeman sublevels. This functionality has enabled quantum sensing in a variety of applications,[1] including atomic scale magnetic resonance imaging of nuclear spin clusters,[4] probing intracellular molecular dynamics,[5] nanometer-scale thermometry with millikelvin accuracy inside a living cell,[6] imaging magnetic fields in live magnetotactic bacteria,[7] measuring local ion concentrations,[8] and strain/pressure sensing.[8] The main downsides of NV^- centers relate to the large bulk of the diamond lattice, the poor control over where the NV^- defects arise in the lattice, and the fixed nature of the NV^- center coherence properties.[9]

Production of molecules exhibiting the same optical initialization and readout capabilities would overcome these limitations of NV^- centers and open up *in situ* and *in vivo* quantum sensing capabilities on the single nanometer scale. Multiple systems have been investigated on the basis of both S = 1 and S > 1 architectures,[10–12] but to date, the most successful molecules have been pseudo-T_d S = 1 Cr(IV) tetraaryl and tetraalkyl complexes.[13,14] However, owing to fast spin relaxation, Cr(IV) molecular qubits do not display spin coherence at temperatures higher than ~60 K, at which point T_m becomes T_1 limited. This behavior is significantly inferior to that of both NV^- centers and microwave addressable S = ½ molecular qubits such as VOPc and $[Cu(mnt)_2]^{2-}$, which display coherence up to room temperature.[15–17] In particular, quantum sensing of biological systems would benefit greatly from the ability to perform room-temperature coherence measurements under ambient biochemical conditions. Therefore, to maximize the full potential of optically addressable molecular qubits, it is essential to identify and remove contributions to fast spin relaxation.

Recently, T_1 anisotropy has emerged as a novel technique for interrogating spin-phonon coupling contributions to spin relaxation and decoherence in S = ½ systems.[18] This approach can provide information regarding the vibrational contributions and mechanism of spin relaxation that is not accessible through more common temperature-dependent T_1 measurements. Here we apply this methodology to an S = 1 tetraaryl Cr(IV) optically addressable molecular qubit. We find qualitatively different T_1 anisotropy patterns relative to copper(II) and oxovanadium(IV) systems, indicating unique spin-phonon coupling contributions to spin relaxation.

The concept of T_1 anisotropy probes how the spin relaxation rate changes for molecules with different orientations relative to the spectrometer's applied magnetic field (B_0). In general, EPR spectra of powder or frozen solution samples can display resonance positions selective for these different molecular orientations, enabling access to orientation-specific relaxation rates without the need for single crystal experiments.[19] Cr(IV) qubits satisfy this requirement for orientation selectivity, as the microwave absorption spectrum of Cr(*o*-tolyl)$_4$ is composed of two transitions between the three M_S sublevels, and each spin transition occurs at a different resonance field depending on the molecular orientation (**Figure 1A-B**). By weighting these orientations with the fraction of molecules absorbing at the given field and averaging over the two spin transitions, we can define an average molecular orientation probed by EPR at any given resonance field (**Figure 1C**). At X-band, the pure parallel position can be addressed by performing pulsed EPR at 220 mT and 480 mT (lines atop **Figure 1A**). While no single position is uniquely selective for the perpendicular orientation, the Pake pattern horns at 280 mT and 410 mT display an average orientation around 80°, giving a close approximation to the pure perpendicular position behavior.

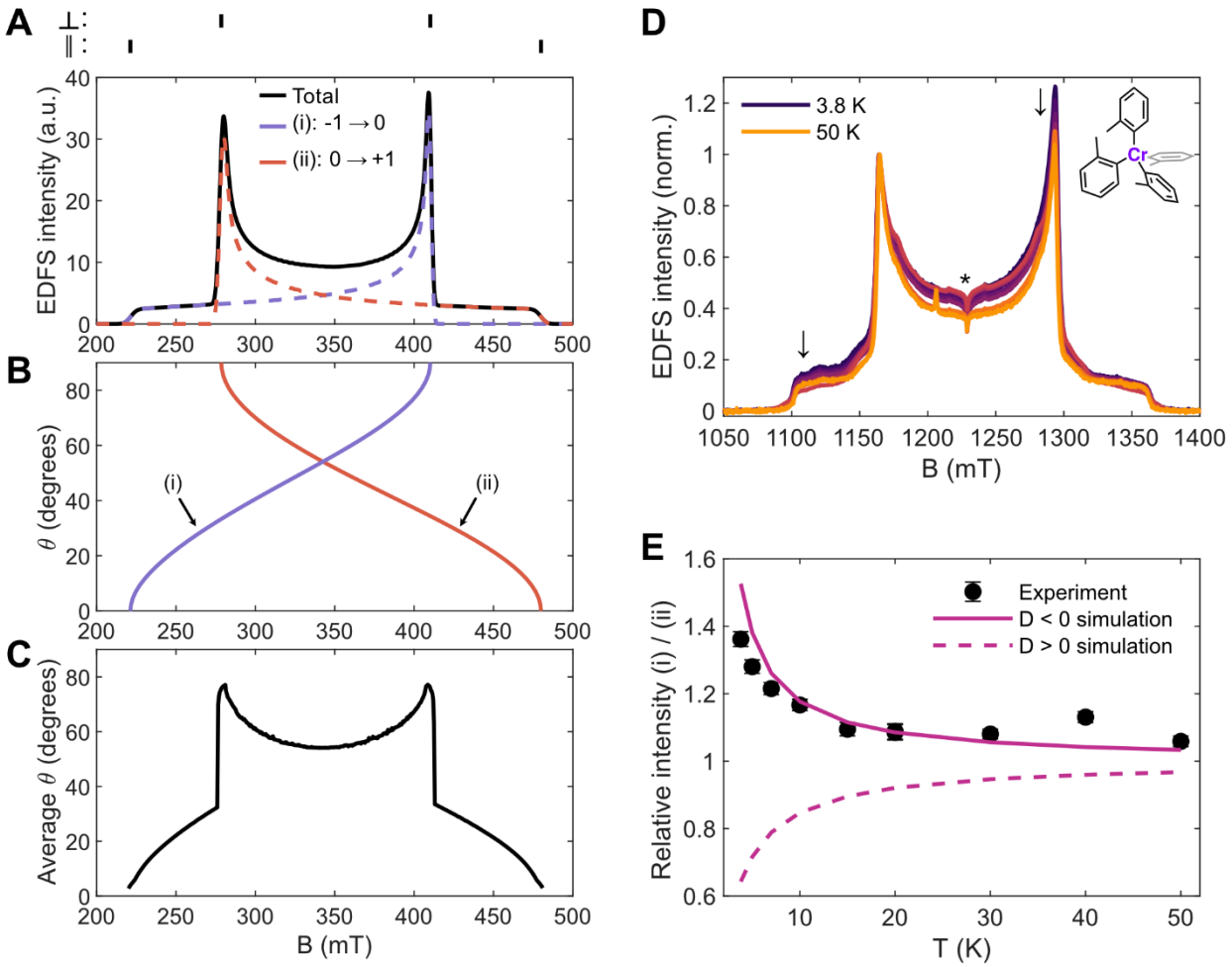

Figure 1. Anisotropy in Cr(IV) pulsed EPR. (A) Simulated X-band EDFS for Cr(*o*-tolyl)$_4$ showing the contributions from each spin transition in the case of $D < 0$. (B) Orientation of the molecule with respect to the value of B_0. $\theta = 0°$ indicates B_0 is parallel to the principal symmetry axis of the axial ZFS tensor. (C) Average orientation of the molecule over all spin transitions. (D) Variable-temperature Q-band EDFSs using soft pulses (π = 80 ns) and normalized to the peak at 1160 mT. * likely indicates an artifact due to cross-relaxation or a double-quantum transition (Supporting Information Section 3). (E) Comparison between experimental powder manifold intensities and simulations for $D < 0$ and $D > 0$.

The identity of the $M_S = -1 \rightarrow 0$ and $M_S = 0 \rightarrow +1$ transitions depends upon the sign of the axial zero-field splitting (ZFS) parameter D, which can be ambiguous in many spectroscopic measurements.[13] Indeed, while the absolute ZFS parameters for Cr(*o*-tolyl)$_4$ have been reported ($|D| = 0.121$ cm^{-1}, $E \approx 0$ cm^{-1})[13], the sign of the ZFS has yet to be determined experimentally. To achieve this, we acquired variable-temperature Q-band echo-detected field sweeps (EDFSs) from 3.8 K – 50 K (**Figure 1D**). Soft microwave

pulses were employed to suppress electron spin echo envelope modulation (ESEEM), which can add artifacts to EDFS spectra, and T_m was measured at several field positions and temperatures to ensure anisotropic T_m did not bias the EDFS intensity (**Supporting Information Sections 3 – 4**). As the sample temperature increases, the intensity of the spin transition spanning 1100 – 1290 mT decreases relative to the transition spanning 1160 – 1370 mT (arrows in **Figure 1D**). This behavior and corresponding simulation (**Figure 1E**) indicates that the former is the ground state $M_S = -1 \rightarrow 0$ transition and that the sign of D is negative for Cr(*o*-tolyl)$_4$ ($D = -0.121$ cm^{-1}), consistent with calculations.[20,21] Note this sign differs from the pseudo-T_d Cr(IV) siloxide complex, Cr(DTBMS)$_4$, which exhibits $D > 0$.[22]

Inversion recovery T_1 measurements at 40 K were conducted on a 1.8% dilution of Cr(*o*-tolyl)$_4$ into an isostructural diamagnetic Sn(*o*-tolyl)$_4$ matrix (**Figure 2A-C**). The slowest rates of spin relaxation were recorded at the pure parallel orientations, while the perpendicular orientations also displayed local minima in the spin relaxation rates (**Figure 2B**). Fastest spin relaxation was observed at the intermediate orientations closest to 45°, which are found both immediately to the outside of the Pake pattern horns and also in the very center of the spectrum (**Figure 1C**). The T_1 anisotropy pattern can be most nearly described by a $\sin^2(2\theta)$ functional form (**Figure 2C**), where θ is obtained from the orientation analysis in **Figure 1**. The $\sin^2(2\theta)$ function accounts for the slower spin relaxation along the canonical (parallel and perpendicular) orientations and faster spin relaxation along the intermediate orientations. Additionally, a $\sin^2(\theta)$ function and a linear function proportional to B (linear in the magnetic field) were considered. Note that the function linear in B does not directly depend upon the molecular angle θ and is therefore more precisely construed as isotropic field-dependent spin relaxation rather than true anisotropy (**Supporting Information Section 5.3**). This term may be understood as the slope of the Brons-van Vleck spin lifetime field dependence commonly observed in AC magnetometry, and this slope is indeed negative at X-band fields (0.3 mT) for common V(IV) qubits.[23] A least-squares fit of the inversion recovery data was conducted to quantify the relative contributions of different anisotropy functions (**Supporting Information Section 5.1** and **5.3**). The 40 K T_1 field dependence of Cr(*o*-tolyl)$_4$ can be described by this method as composed of 13% $\sin^2(2\theta)$, 6% $\sin^2(\theta)$, and 5% linear in B contributions, with a 76% constant (isotropic) component.

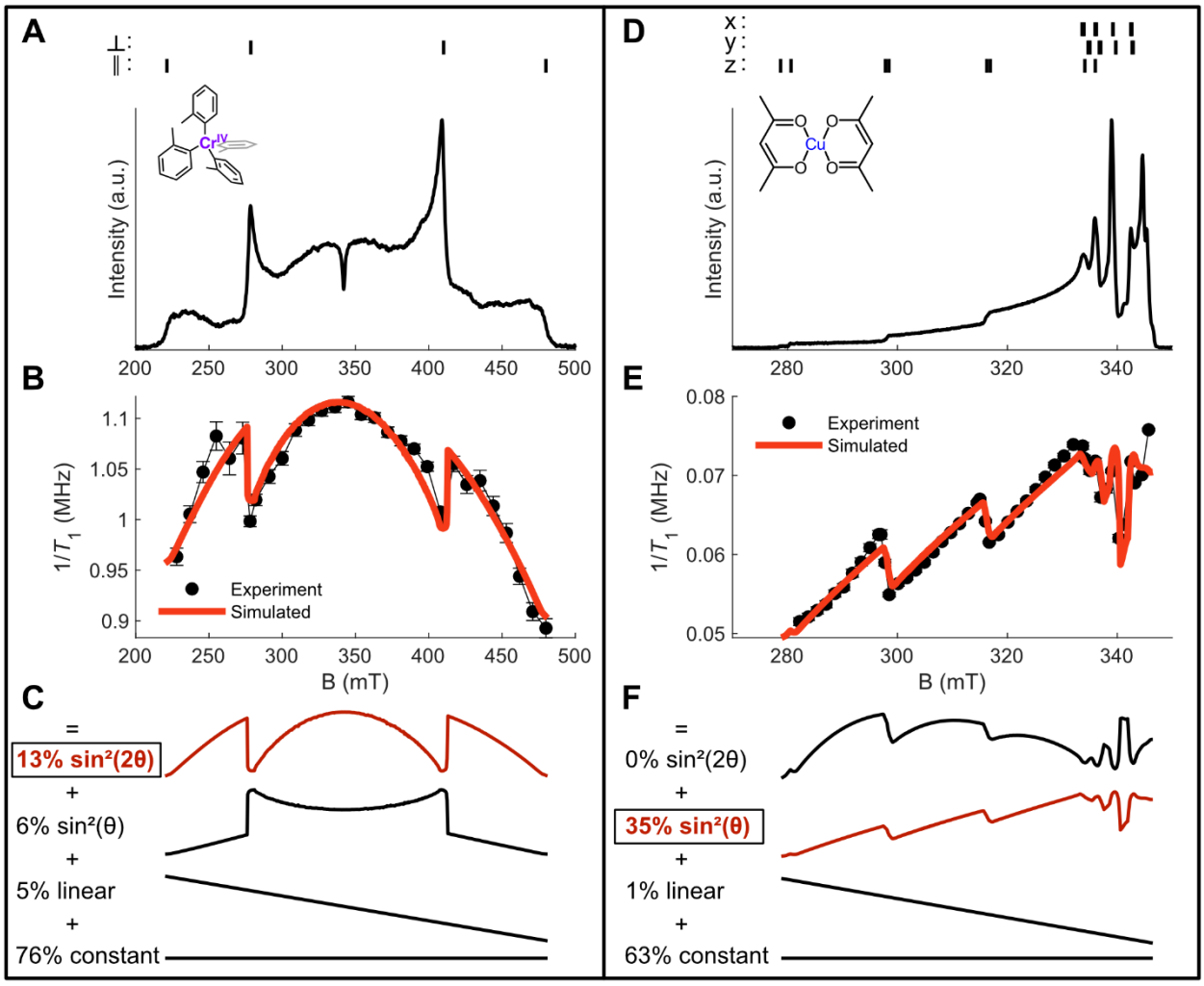

Figure 2. T_1 anisotropy at 40 K of (A-C) Cr(*o*-tolyl)$_4$ and (D-F) Cu(acac)$_2$. (A,D) X-band EDFSs. (B,E) T_1 anisotropy by inversion recovery, overlaid with best fit. (C,F) Orientation functions used to construct the T_1 anisotropy fit.

Crucially, this behavior contrasts with that observed for tetragonal S = ½ Cu(II), V(IV), and Cr(V) compounds previously investigated by T_1 anisotropy at 100 K, in which fastest and slowest values of spin relaxation were always found at the canonical orientations.[18,19,24] To see if this was an effect of the temperature regime studied, we collected T_1 anisotropy at 40 K of 0.1% Cu(acac)$_2$ diluted in the isostructural diamagnetic matrix Pd(acac)$_2$ (**Figure 2D-F**). The 40 K Cu(acac)$_2$ completely follows the $\sin^2(\theta)$ functional form with no apparent significant contributions from $\sin^2(2\theta)$ (**Figure 2F**). The spin

relaxation rate at the 45° orientation is simply the average of the rates at the canonical positions. These observations point to a qualitatively different origin of T_1 anisotropy in Cr(*o*-tolyl)$_4$ vs. Cu(acac)$_2$.

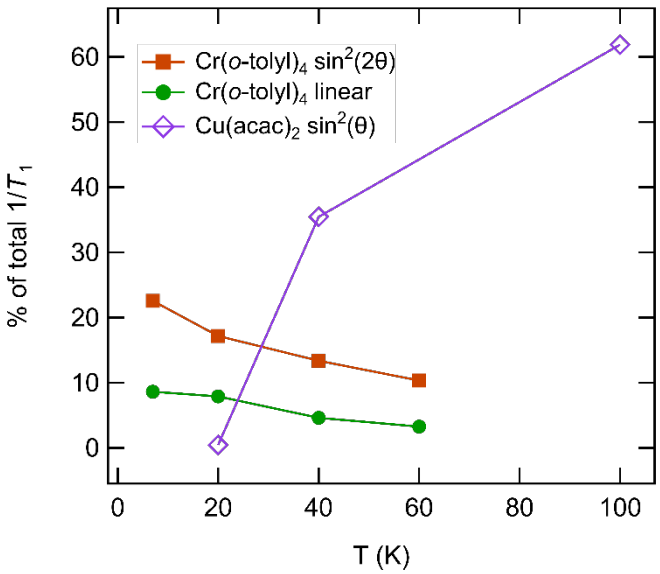

Figure 3. Temperature dependence of T_1 anisotropy contributions for Cr(*o*-tolyl)$_4$ and Cu(acac)$_2$.

To ascertain the type of vibrations responsible for these distinct patterns, we probed the temperature dependence of the T_1 anisotropy for Cr(*o*-tolyl)$_4$ and Cu(acac)$_2$. We quantify the amount of T_1 anisotropy as a fraction of the largest $1/T_1$ over all field positions (**Figure S17**). Over the temperature range 7 K – 60 K, the amount of T_1 anisotropy for Cr(*o*-tolyl)$_4$ steadily decreases, with the dominant $\sin^2(2\theta)$ anisotropic contribution decreasing from 23% to 10% of the total T_1 (**Figure 3**). This decrease with increasing temperature indicates that $\sin^2(2\theta)$ anisotropy arises from very low energy degrees of freedom, likely acoustic or pseudo-acoustic phonons[25] (*vide infra*). Indeed, the isotropic field-dependent contribution to $1/T_1$ decreases at the same pace over this temperature range, and this contribution is commonly ascribed to the direct process of spin relaxation.[23] By contrast, the $\sin^2(\theta)$ T_1 anisotropy contribution increases sharply with temperatures for Cu(acac)$_2$, constituting only 0.5% of the total T_1 at 20 K but 62% at 100 K (**Figure 3**). Examination of the field-dependent T_1 for Cu(acac)$_2$ at 20 K validates that the spin relaxation anisotropy is greatly reduced (**Figure S22**), while the parallel and perpendicular T_1 at 100 K differ by a factor of 2.4,

as observed and analyzed previously by our group.[18] This validates that the $\sin^2(\theta)$ anisotropy for $Cu(acac)_2$ arises from higher energy molecular vibrational modes (optical phonons) that are not thermally populated at 20 K. Thus, the T_1 anisotropies for Cr(*o*-tolyl)$_4$ vs. $Cu(acac)_2$ originate from different types of phonons. Note that both anisotropies are temperature-dependent in a manner consistent with the effect of thermal population of vibrational modes.[26–28] Anisotropic spectral diffusion was ruled out as a principal cause of the observed T_1 patterns for both compounds (**Supporting Information Section 5.2**).

A major attraction of the T_1 anisotropy methodology lies in the possibility of correlating the observed functional forms (*e.g.*, $\sin^2(\theta)$ and $\sin^2(2\theta)$) to their origins in specific molecular degrees of freedom. Previous work has analyzed $\sin^2(\theta)$ spin relaxation anisotropy for Cu(II) and V(IV) molecular vibrations and shown it to be consistent with totally symmetric modes with metal-ligand stretching character[26,29,30] inducing relaxation through a modulation of the minority spin component of the ligand field wavefunction.[18] However, a new theoretical analysis is required to explain the $\sin^2(2\theta)$ anisotropy in Cr(*o*-tolyl)$_4$. While $\sin^2(2\theta)$ T_1 anisotropy has not been previously characterized, T_m anisotropy with a $\sin^2(2\theta)$ functional dependence has been observed in several S = ½ systems and has been attributed to rotational motion caused by librations.[31–33] This induces a change in resonant field position described by $dB_{res}/d\theta$, which is determined by the derivative of the projected g value, $dg/d\theta$. The derivative of the g-tensor dg/dQ has been successfully used as a simplified model for the spin-phonon coupling coefficient describing spin relaxation, where in this case the vibrational mode Q is equal to a rotation θ, so there may be a connection between $dB_{res}/d\theta$ and spin relaxation in this context as well.

We therefore hypothesized that rotational motion from low-energy pseudo-acoustic or acoustic phonons may explain the $\sin^2(2\theta)$ functional form of the Cr(*o*-tolyl)$_4$ T_1 anisotropy. As the ZFS (D = –0.121 cm^{-1}) is smaller than the Zeeman splitting energy at X-band (0.32 cm^{-1} for g = 2 at 340 mT), we assume the spins are aligned along the applied magnetic field and treat the ZFS as a first-order perturbation to the Zeeman splitting of energy levels. Treating $dB_{res}/d\theta$ as a quantity proportional to the spin-flip matrix element for rotational motion, we obtain (**Supporting Information Section 6**):

$$\frac{1}{T_1} \propto \left|\frac{\partial B_{res}}{\partial \theta}\right|^2 = \frac{9D^2}{4\beta^2 g^2}\mathbf{sin^2(2\theta)} \quad (1)$$

Thus, the $\sin^2(2\theta)$ form is consistent with the expected T_1 anisotropy due to rotational motion. The decrease in the $\sin^2(2\theta)$ contribution to the T_1 anisotropy with increasing temperature also suggests that the rotational motion arises from low-energy acoustic or pseudo-acoustic phonons. The latter may carry significant rotational character when there are multiple molecules per unit cell,[25] as is the case here (Z = 10).[34]

The T_1 anisotropy for Cr(*o*-tolyl)$_4$ reduces in magnitude at higher temperatures as molecular vibrations begin to dominate spin relaxation through the Raman process. It remains to be asked why the Cr(*o*-tolyl)$_4$ higher energy (> 100 cm^{-1}) molecular vibrations do not display T_1 anisotropy, while the Cu(acac)$_2$ totally symmetric vibrations display strong $\sin^2(\theta)$ anisotropy. This phenomenon is explained by a consideration of the orbital angular momentum matrix elements for a square planar vs. pseudo-T_d system. For D_{4h} Cu(acac)$_2$, the $d(x^2\text{-}y^2)$ ground state has an orbital angular momentum matrix element with the d(xy) excited state of squared modulus 4, while the matrix elements with d(xz) and d(yz) each have a squared modulus of only 1.[30] These orbital angular momentum matrix elements control the amount of minority spin in the ground state wavefunction. Since the different excited states contribute to the wavefunction's minority spin along only some magnetic field orientations, the total minority spin for Cu(acac)$_2$ is greater for the perpendicular orientation than for the parallel orientation, thus giving rise to anisotropic relaxation.[18] However, in the cubic symmetry of the T_d point group, there can be no difference in matrix elements between the equivalent x, y, and z directions, so there can be no difference in the minority spin along different orientations. The small distortion from T_d required to produce nonzero ZFS[22,35] is evidently too small to yield a significant $\sin^2(\theta)$ T_1 anisotropy in Cr(*o*-tolyl)$_4$. Similar arguments were proposed to rationalize the presence of T_1 anisotropy in tetragonal nitridochromium(V) octaethylporphyrin and nitridochromium(V) tetratolylporphyrin, whereas the rhombic Cr(V)O(HEBA)$_2^-$ complex did not display appreciable T_1 anisotropy.[24,36] Therefore, molecular vibrations (optical phonons) are likely to produce isotropic T_1 for Cr(*o*-tolyl)$_4$, in contrast to the previously analyzed tetragonal S = ½ systems.

In summary, our findings provide the first direct evidence for ascribing features of spin relaxation to specific degrees of freedom in an optically addressable molecular qubit. These degrees of freedom are distinct from the totally symmetric optical phonons implicated in S = ½ microwave addressable molecular systems. As such, these experimental data are critical for defining the nature of spin-phonon couplings and the mechanism of T_1 in theoretical approaches seeking to model spin relaxation lifetimes. We note that the rotational motion contributions analyzed here likely do not dominate spin relaxation rates for T > 60 K, as the anisotropic component of the spin relaxation is reduced at higher temperatures due to the increased role of high energy molecular vibrations (**Figure 3**). Nonetheless, restraining rotational motions for pseudo-T_d Cr(IV) is likely to prolong spin lifetimes. Such structure-function relationships for spin dynamics will be essential for designing molecular optically addressable qubits displaying room temperature coherence.

Supporting Information

The Supporting Information is available free of charge on the ACS Publications website at DOI:

Experimental methods, temperature-dependent EPR fitting, T_1 anisotropy fitting, and theoretical derivation of T_1 anisotropy functional forms.

Acknowledgements

The authors wish to acknowledge Dr. Paul H. Oyala for assistance with EPR spectroscopy and Dr. Erica Sutcliffe for helpful discussions. N.P.K. acknowledges support by the Hertz Fellowship. N.P.K. and K.M.L. both acknowledge support by the National Science Foundation Graduate Research Fellowship Program under Grant No. DGE-1745301. Financial support from the U.S. Department of Energy (DOE), Office of Science, Office of Basic Energy Sciences, Condensed Phase and Interfacial Molecular Science (DE-SC0022089) is gratefully acknowledged.

References

(1) Schirhagl, R.; Chang, K.; Loretz, M.; Degen, C. L. Nitrogen-Vacancy Centers in Diamond: Nanoscale Sensors for Physics and Biology. *Annu. Rev. Phys. Chem.* **2014**, *65* (1), 83–105. https://doi.org/10.1146/annurev-physchem-040513-103659.
(2) Doherty, M. W.; Manson, N. B.; Delaney, P.; Jelezko, F.; Wrachtrup, J.; Hollenberg, L. C. L. The Nitrogen-Vacancy Colour Centre in Diamond. *Phys. Rep.* **2013**, *528* (1), 1–45. https://doi.org/10.1016/j.physrep.2013.02.001.
(3) Fataftah, M. S.; Freedman, D. E. Progress towards Creating Optically Addressable Molecular Qubits. *Chem. Commun.* **2018**, *54* (98), 13773–13781. https://doi.org/10.1039/C8CC07939K.
(4) Abobeih, M. H.; Randall, J.; Bradley, C. E.; Bartling, H. P.; Bakker, M. A.; Degen, M. J.; Markham, M.; Twitchen, D. J.; Taminiau, T. H. Atomic-Scale Imaging of a 27-Nuclear-Spin Cluster Using a Quantum Sensor. *Nature* **2019**, *576* (7787), 411–415. https://doi.org/10.1038/s41586-019-1834-7.
(5) McGuinness, L. P.; Yan, Y.; Stacey, A.; Simpson, D. A.; Hall, L. T.; Maclaurin, D.; Prawer, S.; Mulvaney, P.; Wrachtrup, J.; Caruso, F.; Scholten, R. E.; Hollenberg, L. C. L. Quantum Measurement and Orientation Tracking of Fluorescent Nanodiamonds inside Living Cells. *Nat. Nanotechnol.* **2011**, *6* (6), 358–363. https://doi.org/10.1038/nnano.2011.64.
(6) Kucsko, G.; Maurer, P. C.; Yao, N. Y.; Kubo, M.; Noh, H. J.; Lo, P. K.; Park, H.; Lukin, M. D. Nanometre-Scale Thermometry in a Living Cell. *Nature* **2013**, *500* (7460), 54–58. https://doi.org/10.1038/nature12373.
(7) Le Sage, D.; Arai, K.; Glenn, D. R.; DeVience, S. J.; Pham, L. M.; Rahn-Lee, L.; Lukin, M. D.; Yacoby, A.; Komeili, A.; Walsworth, R. L. Optical Magnetic Imaging of Living Cells. *Nature* **2013**, *496* (7446), 486–489. https://doi.org/10.1038/nature12072.
(8) Schirhagl, R.; Chang, K.; Loretz, M.; Degen, C. L. Nitrogen-Vacancy Centers in Diamond: Nanoscale Sensors for Physics and Biology. *Annu. Rev. Phys. Chem.* **2014**, *65* (1), 83–105. https://doi.org/10.1146/annurev-physchem-040513-103659.
(9) Graham, M. J.; Zadrozny, J. M.; Fataftah, M. S.; Freedman, D. E. Forging Solid-State Qubit Design Principles in a Molecular Furnace. *Chem. Mater.* **2017**, *29* (5), 1885–1897. https://doi.org/10.1021/acs.chemmater.6b05433.
(10) Fataftah, M. S.; Bayliss, S. L.; Laorenza, D. W.; Wang, X.; Phelan, B. T.; Wilson, C. B.; Mintun, P. J.; Kovos, B. D.; Wasielewski, M. R.; Han, S.; Sherwin, M. S.; Awschalom, D. D.; Freedman, D. E. Trigonal Bipyramidal V3+ Complex as an Optically Addressable Molecular Qubit Candidate. *J. Am. Chem. Soc.* **2020**, *142* (48), 20400–20408. https://doi.org/10.1021/jacs.0c08986.
(11) Wojnar, M. K.; Laorenza, D. W.; Schaller, R. D.; Freedman, D. E. Nickel(II) Metal Complexes as Optically Addressable Qubit Candidates. *J. Am. Chem. Soc.* **2020**, *142* (35), 14826–14830. https://doi.org/10.1021/jacs.0c06909.
(12) Lenz, S.; Bamberger, H.; Hallmen, P. P.; Thiebes, Y.; Otto, S.; Heinze, K.; Slageren, J. van. Chromium(III)-Based Potential Molecular Quantum Bits with Long Coherence Times. *Phys. Chem. Chem. Phys.* **2019**, *21* (13), 6976–6983. https://doi.org/10.1039/C9CP00745H.
(13) Bayliss, S. L.; Laorenza, D. W.; Mintun, P. J.; Kovos, B. D.; Freedman, D. E.; Awschalom, D. D. Optically Addressable Molecular Spins for Quantum Information Processing. *Science* **2020**, *370* (6522), 1309–1312. https://doi.org/10.1126/science.abb9352.
(14) Laorenza, D. W.; Kairalapova, A.; Bayliss, S. L.; Goldzak, T.; Greene, S. M.; Weiss, L. R.; Deb, P.; Mintun, P. J.; Collins, K. A.; Awschalom, D. D.; Berkelbach, T. C.; Freedman, D. E. Tunable Cr4+ Molecular Color Centers. *J. Am. Chem. Soc.* **2021**, *143*, 21350–21363. https://doi.org/10.1021/jacs.1c10145.
(15) Bader, K.; Dengler, D.; Lenz, S.; Endeward, B.; Jiang, S.-D.; Neugebauer, P.; van Slageren, J. Room Temperature Quantum Coherence in a Potential Molecular Qubit. *Nat. Commun.* **2014**, *5* (1), 5304. https://doi.org/10.1038/ncomms6304.
(16) Atzori, M.; Tesi, L.; Morra, E.; Chiesa, M.; Sorace, L.; Sessoli, R. Room-Temperature Quantum Coherence and Rabi Oscillations in Vanadyl Phthalocyanine: Toward Multifunctional Molecular Spin Qubits. *J. Am. Chem. Soc.* **2016**, *138* (7), 2154–2157. https://doi.org/10.1021/jacs.5b13408.

(17) Follmer, A. H.; Ribson, R. D.; Oyala, P. H.; Chen, G. Y.; Hadt, R. G. Understanding Covalent versus Spin–Orbit Coupling Contributions to Temperature-Dependent Electron Spin Relaxation in Cupric and Vanadyl Phthalocyanines. *J. Phys. Chem. A* **2020**, *124* (44), 9252–9260. https://doi.org/10.1021/acs.jpca.0c07860.
(18) Kazmierczak, N. P.; Hadt, R. G. Illuminating Ligand Field Contributions to Molecular Qubit Spin Relaxation via T1 Anisotropy. *J. Am. Chem. Soc.* **2022**, *144* (45), 20804–20814. https://doi.org/10.1021/jacs.2c08729.
(19) Du, J.-L.; Eaton, G. R.; Eaton, S. S. Temperature and Orientation Dependence of Electron-Spin Relaxation Rates for Bis(Diethyldithiocarbamato)Copper(II). *J. Magn. Reson. A* **1995**, *117* (1), 67–72. https://doi.org/10.1006/jmra.1995.9971.
(20) Sauza-de la Vega, A.; Pandharkar, R.; Stroscio, G. D.; Sarkar, A.; Truhlar, D. G.; Gagliardi, L. Multiconfiguration Pair-Density Functional Theory for Chromium(IV) Molecular Qubits. *JACS Au* **2022**. https://doi.org/10.1021/jacsau.2c00306.
(21) Janicka, K.; Wysocki, A. L.; Park, K. Computational Insights into Electronic Excitations, Spin–Orbit Coupling Effects, and Spin Decoherence in Cr(IV)-Based Molecular Qubits. *J. Phys. Chem. A* **2022**, *126* (43), 8007–8020. https://doi.org/10.1021/acs.jpca.2c06854.
(22) Bucinsky, L.; Breza, M.; Malček, M.; Powers, D. C.; Hwang, S. J.; Krzystek, J.; Nocera, D. G.; Telser, J. High-Frequency and -Field EPR (HFEPR) Investigation of a Pseudotetrahedral CrIV Siloxide Complex and Computational Studies of Related CrIVL4 Systems. *Inorg. Chem.* **2019**, *58* (8), 4907–4920. https://doi.org/10.1021/acs.inorgchem.8b03512.
(23) Atzori, M.; Morra, E.; Tesi, L.; Albino, A.; Chiesa, M.; Sorace, L.; Sessoli, R. Quantum Coherence Times Enhancement in Vanadium(IV)-Based Potential Molecular Qubits: The Key Role of the Vanadyl Moiety. *J Am Chem Soc* **2016**, *138*, 11234–11244.
(24) Konda, R.; Du, J.-L.; Eaton, S. S.; Eaton, G. R. Electron Spin Relaxation Rates for Nitridochromium(V) Tetratolylporphyrin and Nitridochromium(V) Octaethylporphyrin in Frozen Solution. *Appl. Magn. Reson.* **1994**, *7* (2–3), 185–193. https://doi.org/10.1007/BF03162611.
(25) C. Kragskow, J. G.; Mattioni, A.; K. Staab, J.; Reta, D.; M. Skelton, J.; F. Chilton, N. Spin–Phonon Coupling and Magnetic Relaxation in Single-Molecule Magnets. *Chem. Soc. Rev.* **2023**. https://doi.org/10.1039/D2CS00705C.
(26) Kazmierczak, N. P.; Mirzoyan, R.; Hadt, R. G. The Impact of Ligand Field Symmetry on Molecular Qubit Coherence. *J. Am. Chem. Soc.* **2021**, *143* (42), 17305–17315. https://doi.org/10.1021/jacs.1c04605.
(27) Lunghi, A.; Sanvito, S. The Limit of Spin Lifetime in Solid-State Electronic Spins. *J. Phys. Chem. Lett.* **2020**, *11* (15), 6273–6278. https://doi.org/10.1021/acs.jpclett.0c01681.
(28) Santanni, F.; Albino, A.; Atzori, M.; Ranieri, D.; Salvadori, E.; Chiesa, M.; Lunghi, A.; Bencini, A.; Sorace, L.; Totti, F.; Sessoli, R. Probing Vibrational Symmetry Effects and Nuclear Spin Economy Principles in Molecular Spin Qubits. *Inorg. Chem.* **2021**, *60* (1), 140–151. https://doi.org/10.1021/acs.inorgchem.0c02573.
(29) Mirzoyan, R.; Hadt, R. G. The Dynamic Ligand Field of a Molecular Qubit: Decoherence through Spin–Phonon Coupling. *Phys. Chem. Chem. Phys.* **2020**, *22* (20), 11249–11265. https://doi.org/10.1039/D0CP00852D.
(30) Mirzoyan, R.; Kazmierczak, N. P.; Hadt, R. G. Deconvolving Contributions to Decoherence in Molecular Electron Spin Qubits: A Dynamic Ligand Field Approach. *Chem. – Eur. J.* **2021**, *27*, 9482–9494. https://doi.org/10.1002/chem.202100845.
(31) Du, J.-L.; More, K. M.; Eaton, S. S.; Eaton, G. R. Orientation Dependence of Electron Spin Phase Memory Relaxation Times in Copper(II) and Vanadyl Complexes in Frozen Solution. *Isr. J. Chem.* **1992**, *32* (2–3), 351–355. https://doi.org/10.1002/ijch.199200041.
(32) Jackson, C. E.; Lin, C.-Y.; van Tol, J.; Zadrozny, J. M. Orientation Dependence of Phase Memory Relaxation in the V(IV) Ion at High Frequencies. *Chem. Phys. Lett.* **2020**, *739*, 137034. https://doi.org/10.1016/j.cplett.2019.137034.

(33) Eaton, S. S.; Eaton, G. R. Relaxation Mechanisms. In *eMagRes*; Wiley, 2016; pp 1543–1556. https://doi.org/10.1002/9780470034590.emrstm1507.
(34) Bayliss, Samuel; Laorenza, Daniel; Mintun, Peter; Kovos, Berk; Freedman, Danna; Awschalom, David. CCDC 1992356: Experimental Crystal Structure Determination. https://doi.org/10.5517/CCDC.CSD.CC24W6KT.
(35) Mowat, W.; Shortland, A. J.; Hill, N. J.; Wilkinson, G. Elimination Stabilized Alkyls. Part II. Neopentyl and Related Alkyls of Chromium(IV). *J. Chem. Soc. Dalton Trans.* **1973**, No. 7, 770–778.
(36) Du, J. L.; Eaton, G. R.; Eaton, S. S. Electron-Spin-Lattice Relaxation in Natural Abundance and Isotopically Enriched Oxo-Chromium(V)Bis (2-Hydroxy-2-Ethylbutyrate). *J. Magn. Reson. A* **1995**, *115* (2), 236–240. https://doi.org/10.1006/jmra.1995.1172.

For Table of Contents Only: